

A Constitutive Model for the Formation of Martensite in Austenitic Steels Under Large Strain Plasticity

Håkan Hallberg*, Paul Håkansson and Matti Ristinmaa

Division of Solid Mechanics
Lund University, Box 118, S-221 00 Lund, Sweden
*hakan.hallberg@solid.lth.se

Abstract

A constitutive model for diffusionless phase transitions in elastoplastic materials undergoing large deformations has been developed. The model is formulated with starting-point in basic thermodynamic relations and the phase transition is treated through an internal variable (i.e. the phase fractions) approach. The usual yield potential is used together with a transformation potential to describe the evolution of the new phase. A numerical implementation of the model is presented, complete with the derivation of a consistent algorithmic tangent moduli. Simulations based on the presented model are compared to experimental findings with good agreement. The proposed model offers a robust tool, suitable for large-scale simulations of phase transformations in austenitic steels undergoing extensive deformations. This is demonstrated in simulations of the necking of a bar under tensile loading and also in simulations of a cup deep-drawing process.

Keywords: Phase transformation, constitutive model, large strain plasticity.

1 Introduction

Phase transitions in metallic materials can be subdivided into two main groups: transitions based on redistribution of such micro-constituents as carbon by means of diffusional processes and transitions proceeding entirely by way of rearrangement of the crystal lattice. The former category includes the formation of pearlite and bainite in austenitic steels. These processes are slow, due to the time-consuming diffusion process involved. The latter

category includes the formation of bct martensite (α') from an austenitic fcc parent phase (γ). The formation of martensite can proceed through the material at the speed of sound, the transition thus being more or less instantaneous. The transition from austenite to martensite can be induced both by changes in temperature and by variations in the stress- or strain-state of the material. The growth of the martensite phase is strongly dependent on the temperature. An elevated temperature restrains the martensite growth while lower temperatures promote it.

Phase transitions in metals have a major influence on the material behavior in several common engineering applications. Shape memory alloys (SMA:s) and steels exhibiting enhanced response to transformation-induced plasticity (TRIP-steels) are two examples of the important role martensite formation can play. Such production processes as bulk metal forging and the forming of sheet metal are other areas in which the transition of austenite into martensite is highly important.

Beginning with some historical notes, it is shown in the early work of Greenwood and Johnson (1965) that the progression of a phase transition in a material is able to induce plastic straining, even though temperature and loading stress are kept constant. The so-called Greenwood-Johnson effect describes how the difference in volume between two co-existing phases induces yielding in the weaker of the two phases. Plastic flow is thus permitted despite the externally applied load being in itself insufficient to induce plasticity in the material. Phase transitions were also addressed by Magee (1969), who showed that external loading can trigger martensite formation in preferred directions. These preferred directions cause an orientation effect that influences the macroscopic shape of the loaded body. The Greenwood-Johnson mechanism and the Magee effect indicate that the material undergoing martensitic phase transition will exhibit both a volumetric and a deviatoric response along with directional dependency.

Several models of the diffusionless phase transition of austenite into martensite have been proposed. These models can be classified in terms of those based on crystallographic – i.e. microscopic – descriptions and those dealing with the phase transition in continuum mechanical – i.e. macroscopic – terms. In the present work, in which we follow the latter path, a continuum mechanical model is developed.

Olson and Cohen (1975) presented an early model describing the kinetics of a strain-induced martensitic phase transition. The model is based on an estimation of the number of martensite nucleation sites present in the material and the subsequent probability of nucleation at these sites. Stringfellow *et al.* (1992) later modified the Olson-Cohen model to also take the stress-state into account. Another early model of martensite formation in austenitic carbon steels and ferrous alloys was presented by Koistinen and Marburger (1959). Their model has also served as the starting point for several modifications of later date, primarily focused on incorporating the influence of the stress-state into the model. Models such as these are often presented together with an explicit relationship describing

the evolution of the martensitic phase in the material.

Among the more recent models – in which martensite formation has been studied extensively – the works of Leblond (1980), Sjöström (1982), Sjöström (1985), Leblond *et al.* (1986a,b), Leblond *et al.* (1989); Leblond (1989), Tanaka *et al.* (1994), Tanaka *et al.* (1996), Fischer *et al.* (1997), Petit-Grostabussiat *et al.* (2004), Idesman *et al.* (2005), Turteltaub and Suiker (2005) and Wolff *et al.* (2006) should be mentioned. Leblond *et al.* (1989) and Leblond (1989) discuss the evolution of strain due to phase transition. The evolution is derived in phenomenological terms and it is assumed to be coaxial with the stress applied and to be proportional to the transformation rate. The Magee effect, i.e. transformation in preferred directions, is consequently not considered by these authors. The Greenwood-Johnson effect is also discussed from a micromechanical perspective by Taleb and Sidoroff (2003), with references to Leblond and co-authors. Tomita and Iwamoto (1995, 2001) presents a model based on the work of Stringfellow *et al.* (1992), one which features a strain evolution similar to that of Leblond (1989) and Leblond *et al.* (1989) and also an evolution of the martensite transformation based on the theory of Olson and Cohen (1975). In Tomita and Iwamoto (2001) and in Iwamoto and Tsuta (2002) the influence of both the second and the third invariant of the deviatoric stress tensor is considered.

Knowledge of the microscopic transformation strain in a micro-region can also be used, following a homogenization procedure, to determine the macroscopic transformation strain, such as in the models of Simonsson (1994), Levitas (1997), Fischer *et al.* (1998), Fischer *et al.* (2000), Cherkaoui *et al.* (2000), Levitas *et al.* (2002) and Garion *et al.* (2006). As a further example, the model of Levitas *et al.* (1998) can be mentioned. Here a multiplicative decomposition of the deformation gradient is made possible on a micromechanical level due to knowledge of the crystal orientations. The benefit of the micromechanical approach is the possibility it provides of accurately predicting both the Greenwood-Johnson mechanism and the Magee effect. It is quite difficult, however, to determine the transformation strain in a micro-region, especially in the case of common stainless steel.

The model proposed in the present paper is based on fundamental thermodynamic concepts and it includes large deformations through the introduction of a stress-free intermediate configuration. This permits a multiplicative decomposition of the deformation gradient into an elastic, recoverable, part and an irreversible part, cf. Kröner (1960) and Lee and Liu (1967). The irreversible part includes both a plastic deformation in the form of slip and a deformation due to phase transformation. The proposed model is furthermore conveniently implemented and quite effectively calibrated against experimental data to accommodate several effects of martensitic transformation encountered in practice. The evolution of these deformations is defined by the yield potential function found in classical J_2 -plasticity in combination with a transformation potential function. Identifying the thermodynamic forces that drive the phase-front through the material allows the evolution of the phase transition to be described. The use of a transformation potential, which also serves as a

transformation condition, is based on the assumption that a transformation takes place if it leads to a decrease in Gibbs free energy, cf. Ganghoffer *et al.* (1991a), Ganghoffer *et al.* (1991b), Fischer *et al.* (1997, 1998) and Turteltaub and Suiker (2005). The particular form of transformation potential adopted here results in an evolution of the transformation deformation similar to that adopted by Tomita and Iwamoto (2001). Treating plastification and phase transition in this way allows a coherent model to be developed. Since the present model is formulated in a continuum mechanical framework, the Greenwood-Johnson and Magee mechanisms will be phenomenologically addressed through the macroscopic homogenization of micromechanical effects. The goal of the present formulation is an effective constitutive model suitable for large-scale simulations of finite strain processes. The model should furthermore be conveniently calibrated and easily implemented

The first section of the paper provides a brief overview of the basic kinematic relations and definitions used throughout the remainder of the text. A general account is provided then of the thermodynamical basis of the model. The section following that describes the specific model used in subsequent simulations. Descriptions are provided of the yield and transformation potential functions and the evolution laws for the internal variables, in a manner allowing the constitutive model to be specified. The last part of the paper is devoted to an account of model calibration procedures and illustrative numerical simulations in which the capabilities of the proposed model are demonstrated.

2 Kinematics

Let $\Omega_0 \subset \mathbb{R}^3$ denote the reference configuration of a given body, the particles being labeled as $\mathbf{X} \in \Omega_0$, and let $\varphi_t(\mathbf{X})$ denote the nonlinear deformation map which maps the reference configuration Ω_0 , for each point in time t onto the current configuration $\Omega = \varphi_t(\Omega_0) \subset \mathbb{R}^3$. The position of the particle labeled $\mathbf{X} \in \Omega_0$ at time t is given as $\mathbf{x} = \varphi_t(\mathbf{X}) \equiv \varphi(\mathbf{X}, t)$. The linear tangent map $\mathbf{F} = \nabla_{\mathbf{X}}\varphi_t$ – which denotes the deformation gradient – transforms the tangent vectors of Ω_0 to tangent vectors on Ω . \mathbf{F} thus defines a linear mapping between the tangent spaces of the two configurations. The determinant J of the deformation gradient, which corresponds to the local change in volume, is given by $J = \det(\mathbf{F}) \equiv \rho_0/\rho$, where ρ_0 and ρ denotes the density in the reference and in the current configuration, respectively.

A time differentiation of the deformation gradient allows the spatial velocity gradient to be defined as

$$\mathbf{l} = \dot{\mathbf{F}}\mathbf{F}^{-1} \tag{1}$$

where the superposed dot denotes the material time derivative and $(\cdot)^{-1}$ denotes the inverse. To allow for the modeling of an inelastic response, a multiplicative split of the deformation

gradient into an elastic part and an irreversible part is adopted, cf. Kröner (1960) and Lee and Liu (1967). The resulting decomposition is then given as

$$\mathbf{F} = \mathbf{F}^e \mathbf{F}^{ir} \quad (2)$$

where the superscripts e and ir denote the elastic and the irreversible (i.e. plastic and transformational) components, respectively. This decomposition is further discussed by e.g. Levitas *et al.* (1998). Using the previous multiplicative split of the deformation gradient, one can then write

$$\mathbf{l} = \mathbf{l}^e + \mathbf{F}^e \bar{\mathbf{l}}^{ir} \mathbf{F}^{e-1} \quad (3)$$

where in accordance with (1) the following notations for the elastic and the irreversible parts of the velocity gradient, respectively, are introduced

$$\mathbf{l}^e = \dot{\mathbf{F}}^e \mathbf{F}^{e-1}, \quad \bar{\mathbf{l}}^{ir} = \dot{\mathbf{F}}^{ir} \mathbf{F}^{ir-1} \quad (4)$$

The following spatial quantity to be used later on is also introduced:

$$\mathbf{l}^{ir} = \mathbf{F}^e \bar{\mathbf{l}}^{ir} \mathbf{F}^{e-1} \quad (5)$$

The multiplicative split of the deformation gradient is closely connected with the definition of a stress-free, unloaded, intermediate configuration via the mapping \mathbf{F}^e . Since only isotropy will be considered here and a spatial description will be utilized, it will not be necessary to consider such properties as the definition of anisotropy and its evolution in relation to the intermediate configuration. For these matters, the reader is referred to Harrysson and Ristinmaa (2006).

3 Thermodynamical basis

The model to be considered will be derived within a thermodynamic framework in which the second law of thermodynamics plays an important role. Since only isothermal processes are considered, the second law of thermodynamics can be written in the form of a dissipation inequality as

$$\mathcal{D} = \boldsymbol{\tau} : \mathbf{d} - \rho_0 \dot{\psi} \geq 0 \quad (6)$$

where $\boldsymbol{\tau}$ is the Kirchhoff stress tensor, ψ the Helmholtz free energy function and $\mathbf{d} = \text{sym}(\mathbf{l})$, the rate-of-deformation tensor. Note that $\text{sym}(\cdot)$ denotes the symmetric part of a tensorial quantity and $(\cdot) : (\cdot)$ the inner tensor product over two indices. The set of state variables considered consists of the elastic left Cauchy-Green tensor $\mathbf{b}^e = \mathbf{F}^e \mathbf{F}^{eT}$, the isotropic hardening parameters κ_i , the absolute temperature θ and the volume fraction

of martensite $z \in [0, 1]$ where $z = 0$ indicates only austenite to be present while $z = 1$ indicates only martensite to be found. Only the transition of the austenite phase into martensite, i.e. the increase in the value of z , will be discussed here. The hardening behavior of the material – as controlled by the internal variables κ_i – will include both hardening due to plastic slip, i.e. increased dislocation density, and also the contribution from an evolving martensitic phase. The latter is included through a mixture law, as discussed below, combining the yield stresses of the two co-existing phases. With use of these internal variables, the free energy becomes $\psi = \psi(\mathbf{b}^e, \kappa_i, z, \theta)$. Note that for the isothermal situation considered here the temperature is treated as a parameter. Taking advantage of both (3) and (4), the dissipation inequality (6) can be rewritten as

$$\mathcal{D} = \boldsymbol{\tau} : \text{sym}(\mathbf{l}^{ir}) - \sum_i R_i \dot{\kappa}_i - Q \dot{z} \geq 0 \quad (7)$$

where it is used that the Kirchhoff stress tensor, cf. Simo and Hughes (2000), is defined as

$$\boldsymbol{\tau} = 2\rho_0 \frac{\partial \psi}{\partial \mathbf{b}^e} \mathbf{b}^e \quad (8)$$

and that isotropy is being considered, i.e. that the Helmholtz free energy function is an isotropic function of \mathbf{b}^e , which makes $\boldsymbol{\tau}$ and \mathbf{b}^e commute. The following definitions are also introduced:

$$R_i = \rho_0 \frac{\partial \psi}{\partial \kappa_i}, \quad Q = \rho_0 \frac{\partial \psi}{\partial z} \quad (9)$$

where R_i and Q are thermodynamic forces, cf. e.g. Müller and Bruhns (2006). With use of the expression (7), the dissipation considered can be conceptually subdivided into plastic, \mathcal{D}^p , and transformational, \mathcal{D}^{tr} , parts according to

$$\mathcal{D}^p = \boldsymbol{\tau} : \text{sym}(\mathbf{l}^p) - \sum_i R_i \dot{\kappa}_i \geq 0, \quad \mathcal{D}^{tr} = \boldsymbol{\tau} : \text{sym}(\mathbf{l}^{tr}) - Q \dot{z} \geq 0 \quad (10)$$

In order to achieve this convenient split, use is made of the notation given by (3) and (4), which allows \mathbf{l}^{ir} to be decomposed into a plastic part \mathbf{l}^p and a transformation-related part \mathbf{l}^{tr} according to

$$\mathbf{l}^{ir} = \mathbf{l}^p + \mathbf{l}^{tr} \quad (11)$$

The above split turns out to be the key ingredient in defining a model in which both plasticity and phase transition are present. Taking advantage of (10) a thermodynamically allowable set of evolution laws can be derived. According to traditional plasticity, a domain $\mathcal{P}(z, \theta)$ is defined as

$$\mathcal{P}(z, \theta) = \{(\boldsymbol{\tau}, R_i) \mid f(\boldsymbol{\tau}, R_i, z, \theta) \leq 0\} \quad (12)$$

where f is known as the yield function. The boundary of $\mathcal{P}(z, \theta)$, i.e. $f = 0$, in the stress space is referred to as the yield surface. Note that, in contrast to classical plasticity, $\mathcal{P}(z, \theta)$ does not define a purely elastic region, since phase transition is permitted to take place within $\mathcal{P}(z, \theta)$. In order for the dissipation inequality (10a) to be fulfilled, it is postulated that the evolution laws are governed by a convex potential function $g(\boldsymbol{\tau}, R_i, z, \theta)$ of $\boldsymbol{\tau}$ and R_i such that $g(\boldsymbol{\tau}, R_i, z, \theta) - g(\mathbf{0}, 0, z, \theta) \geq 0$. The evolution laws are then given by

$$\begin{aligned} \text{sym}(\mathbf{l}^p) &= \lambda \frac{\partial g}{\partial \boldsymbol{\tau}} \\ \dot{\kappa}_i &= -\lambda \frac{\partial g}{\partial R_i} \end{aligned} \tag{13}$$

The above formula is referred to as non-associated plasticity, associated plasticity being obtained for the choice of $g = f$. In associated plasticity, the evolution laws follow directly from (10a) with use of the postulate of maximum dissipation. In addition to the evolution laws (13), the Kuhn-Tucker conditions $\lambda \geq 0$, $f \leq 0$ and $\lambda f = 0$ apply.

Consider next the evolution laws related to the dissipation inequality (10b), which define phase transition. From a physical standpoint, the evolution of \mathbf{l}^{tr} must clearly be driven by the rate of the phase transformation, denoted here as \dot{z} . Accordingly, the following must hold:

$$\mathbf{l}^{tr} = \mathbf{h}(\boldsymbol{\tau}, \kappa_i, z, \theta) \dot{z} \tag{14}$$

This generalized format includes the models proposed by Leblond (1980), Giusti (1981) and Sjöström (1982). Taking advantage of (14) in (10b) results in a modified form of the dissipation inequality;

$$\mathcal{D}^{tr} = F \dot{z} \geq 0 \quad \text{where} \quad F = \boldsymbol{\tau} : \mathbf{h} - Q \tag{15}$$

An important observation is provided by (15), namely that F is conjugated to the transformation rate \dot{z} and can be viewed as the thermodynamic force that drives the phase front through the material. In (15), $\boldsymbol{\tau} : \mathbf{h}$ and Q are denoted as the mechanical and the chemical parts of the driving force F , respectively.

The evolution law for the phase transition will be derived in analogy to derivation of the laws for plasticity, and the domain $\mathcal{T}(\theta)$ being defined as

$$\mathcal{T}(\theta) = \{(F, z) \mid h(F, z, \theta) \leq 0\} \tag{16}$$

where h is referred to as the transformation potential function. The evolution law for the transformation part is taken to be

$$\dot{z} = \mu \frac{\partial h}{\partial F} \tag{17}$$

for which the following Kuhn-Tucker conditions are assumed to hold

$$\mu \geq 0, \quad h \leq 0, \quad \mu h = 0 \quad (18)$$

For the dissipation inequality (15) to be fulfilled in the situation considered here, it suffices to assume that $h = F - F_{trans}(z, \theta)$, where $F_{trans}(z, \theta)$ is an experimentally determined function that has the physical meaning of a barrier against phase transformation, and it is then required that $F \geq 0$. With the two domains defined by (12) and (16), respectively, a purely elastic domain can then be defined as

$$\mathcal{E} = \mathcal{P} \cap \mathcal{T} \quad (19)$$

It is concluded that phase transition can take place within \mathcal{P} also when no plastic strains develop. It can also be concluded that a plastic response can occur within the domain \mathcal{T} also when no transformation strains are developed.

4 Specific model

In examining the isotropic model referred to above, consider a form of the Helmholtz free energy function ψ per unit mass in which

$$\rho_0 \psi(\mathbf{b}_i^e, J^e, \kappa, z, \theta) = \rho_0 \psi^e(\mathbf{b}_i^e, J^e, z, \theta) + \rho_0 \psi^{ir}(\kappa, z, \theta) \quad (20)$$

where a subscript i denotes isochoric quantities. ψ^e is related to the hyperelastic part and ψ^{ir} to the hardening part of the model, and the quantities J^e and \mathbf{b}_i^e are

$$J^e = \det(\mathbf{F}^e) \quad \text{and} \quad \mathbf{b}_i^e = J^{e-\frac{2}{3}} \mathbf{b}^e \quad (21)$$

denoting the elastic Jacobian and the isochoric elastic left Cauchy-Green tensor, respectively, and where κ is an internal variable related to the macroscopic effective plastic strain and z , as usual, is the volume fraction of martensite. Since two phases are present – austenite and martensite – there is a mixture of the two. Assuming that the two phases have the same mass densities, the simplest rule that can be applied is given by a linear mixture rule, $\rho_0 \psi = (1 - z) \rho_0 \psi_a + z \rho_0 \psi_m$. Since its use can lead to unsatisfactory results, one can instead introduce a function $m(z)$ such that $m(0) = 0$ and $m(1) = 1$, allowing the following more general mixture rule to be obtained as

$$\rho_0 \psi = [1 - m(z)] \rho_0 \psi_a + m(z) \rho_0 \psi_m \quad (22)$$

in which each phase is assumed to be decoupled according to (20). Note that here and throughout the paper the subscripts a and m refer to the austenite and the martensite

phase, respectively. Since these two phases exhibit similar elastic behavior, it will be assumed that $\psi_a^e = \psi_m^e$. Accordingly, the following form for ψ^e is adopted

$$\rho_0\psi^e = \frac{1}{2}K_{bulk} \left[\frac{1}{2} (J^{e2} - 1) - \ln (J^e) \right] + \frac{1}{2}G_{shear} [\text{tr}(\mathbf{b}_i^e) - 3] \quad (23)$$

where the material parameters K_{bulk} and G_{shear} correspond to the initial bulk and the shear moduli, respectively. Observe that the notation $\text{tr}(\cdot)$ has been introduced to denote the trace of a tensorial quantity. With this choice of energy function, the Kirchhoff stress tensor given by (8) takes the form

$$\boldsymbol{\tau} = \frac{1}{2}K_{bulk} (J^{e2} - 1) \mathbf{1} + G_{shear} \mathbf{b}_i^{e,dev} \quad (24)$$

in which a superscript $(\cdot)^{dev}$ denotes the deviatoric part of a quantity and $\mathbf{1}$ is the second-order identity tensor. For the hardening part of the Helmholtz free energy function it can be assumed that

$$\rho_0\psi^{ir} = \frac{1}{2} [1 - m(z)] H_a \kappa^2 + \frac{1}{2} m(z) H_m \kappa^2 \quad (25)$$

where the hardening parameters H_a and H_m are related to the hardening moduli for austenite and martensite, respectively, in the plastic region. From (9) it follows then that

$$R = [1 - m(z)] H_a \kappa + m(z) H_m \kappa \quad \text{and} \quad Q = \frac{1}{2} \frac{dm}{dz} (H_m - H_a) \kappa^2 \quad (26)$$

The thermodynamic force R is used to describe the hardening behavior, in the plastic region, of the material and Q is the chemical force connected with the phase transformation.

In modeling the plastic response, it is assumed that the yield function is of the von Mises-type

$$f(\boldsymbol{\tau}, R, z, \theta) = \sigma_{eff} - \sigma_y(R, z, \theta) \quad (27)$$

where the von Mises effective stress is defined as $\sigma_{eff} = \sqrt{3J_2}$ and the invariant $J_2 = \frac{1}{2}\text{tr}(\boldsymbol{\tau}^{dev}\boldsymbol{\tau}^{dev})$. The yield stress $\sigma_y(R, z, \theta)$ is assumed to be

$$\sigma_y(R, z, \theta) = \sigma_{y0}(z, \theta) + R(\kappa, z) \quad (28)$$

The total homogenized initial yield stress is denoted by $\sigma_{y0}(z, \theta)$ and $R(\kappa, z)$ describes the hardening behavior. When martensite is formed in the austenitic parent phase the material becomes inhomogeneous in the sense that the two phases exhibit differing yield stresses. A frequently used remedy for this is to apply a homogenization process allowing calibration against uniaxial test data to be performed. In the present case, a linear mixture

law was found to yield unsatisfactory model predictions and instead – as already indicated – the initial yield stress is taken as a combination of the yield stresses of austenite and of martensite in accordance with the mixture rule used in (22) such that

$$\sigma_{y0}(z, \theta) = [1 - m(z)] \sigma_{y0}^a + m(z) \sigma_{y0}^m \quad (29)$$

This relation together with (28) provides

$$\sigma_y = [1 - m(z)] (\sigma_{y0}^a + H_a \kappa) + m(z) (\sigma_{y0}^m + H_m \kappa) \quad (30)$$

where it is assumed that $m = m(z)$ is a non-linear relationship which, as will be shown, is determined by model calibration, giving the above relationship. Homogenization performed in this way is used e.g. by Petit-Grostabussiat *et al.* (2004) and non-linear relations such as the one proposed in the present model are discussed e.g. by Leblond *et al.* (1986b). In addition, the potential function used for the evolution laws is chosen as

$$g(\boldsymbol{\tau}, R, z, \theta) = f(\boldsymbol{\tau}, R, z, \theta) + \frac{1}{2} \frac{R^2(\kappa, z)}{R_\infty} \quad (31)$$

As can be shown, this particular choice will lead to an exponential type of hardening in the stress-strain response of the material. From the evolution laws (13) it follows that

$$\begin{aligned} \text{sym}(\mathbf{l}^p) &= \lambda \frac{3 \boldsymbol{\tau}^{dev}}{2 \sigma_{eff}} \\ \dot{\kappa} &= \lambda \left(1 - \frac{R}{R_\infty} \right) \end{aligned} \quad (32)$$

This allows the effective plastic strain to be identified as the plastic multiplier, i.e. as

$$\dot{\varepsilon}_{eff}^{pl} = \left[\frac{2}{3} \text{sym}(\mathbf{l}^p) : \text{sym}(\mathbf{l}^p) \right]^{\frac{1}{2}} = \lambda \quad (33)$$

The hardening behavior of the model is described by (32b), which together with (26a) can be written as

$$\frac{\dot{\kappa}}{1 - \frac{H}{R_\infty} \kappa} = -\dot{\varepsilon}_{eff}^{pl} \quad \text{where} \quad H = [1 - m(z)] H_a + m(z) H_m \quad (34)$$

For fixed values of z , i.e. when no phase transformation occurs, or for the situation in which $H_a = H_m$, the integration of (34) can be carried out explicitly, providing

$$\kappa = \frac{R_\infty}{H} \left[1 - \exp \left(-\frac{H}{R_\infty} \varepsilon_{eff}^{pl} \right) \right] \quad (35)$$

an exponential type of hardening thus being obtained, cf. (35). For the more general case of a non-constant H , however, no explicit form can be obtained.

Consider finally the phase transformation. From (15) it is known that the phase transformation is driven by the thermodynamic force $F = \boldsymbol{\tau} : \mathbf{h} - Q$. To evaluate this expression for the thermodynamic force, we assume a transformation potential on the form

$$h(F, z, \theta) = F - F_{trans}(z, \theta) = 0 \tag{36}$$

The assumed evolution law for z , as defined in (17), together with (36), results in

$$\dot{z} = \mu \tag{37}$$

If (36) is compared with an ordinary yield function for plastic deformation, such as (27), $F_{trans}(z, \theta)$ can be interpreted as a threshold, much like the initial yield stress and some kind of hardening. The threshold value – or transformation barrier – is closely connected with the energy level which develops when a micro-region of austenite is transformed into martensite, while the hardening originates from the homogenization of a volume element which consists of both austenitic and martensitic micro-regions. The hardening function incorporates in a phenomenological way the fluctuations in stress that occur in the heterogeneous volume element. Since the volume fraction of martensite must obey $z \leq 0$, the transformation threshold value $F_{trans}(z, \theta)$ must asymptotically approach infinity as z approaches 1.

Returning to the question of the specific format for h , instead of postulating a specific expression for the transformation strain tensor \mathbf{l}^{tr} providing \mathbf{h} to obtain the form of h , it turns out to be more advantageous to consider a form for h first and from this identify the corresponding evolution law for \mathbf{l}^{tr} . This approach is also more natural from a crystallographic point of view that, later on, is adopted in the calibration procedure. To illustrate this approach, assume that (14) is derived from a potential function \bar{F} that is a homogeneous function of degree one in $\boldsymbol{\tau}$. This gives

$$\boldsymbol{\tau} : \mathbf{h} = \boldsymbol{\tau} \frac{\partial \bar{F}}{\partial \boldsymbol{\tau}} = \bar{F} \tag{38}$$

which allows (36) to be written as

$$h = \bar{F} - Q - F_{trans} \tag{39}$$

Since only \bar{F} is a function of $\boldsymbol{\tau}$, and recalling (10b), an associated form of evolution law for \mathbf{l}^{tr} can be written as

$$\text{sym}(\mathbf{l}^{tr}) = \dot{z} \frac{\partial h}{\partial \boldsymbol{\tau}} \tag{40}$$

Note that both Q and F_{trans} act as barrier functions and that the function $\bar{F}(\boldsymbol{\tau}, z, \theta)$ will determine the shape of the transformation surface in the stress space. One of the most simple functions would be $\bar{F} = \sqrt{3J_2}$, which would form a cylinder in the stress space. Both micromechanical studies and experimental tests have shown, however, that the transformation surface depends on the third deviatoric stress invariant and the level of hydrostatic stress. A candidate for the transformation potential h in (36) is given by

$$h = K \left(\bar{\sigma}_{eff} + \frac{1}{3} \delta I_1 \right) - Q - F_{trans}(z, \theta) = 0 \quad (41)$$

where K and δ are material parameters that can be temperature-dependent. K is similar to the ‘‘Greenwood-Johnson’’-constant used by Berveiller and Fischer (1997). The hydrostatic stress is included through the first stress invariant $I_1 = \text{tr}(\boldsymbol{\tau})$. The quantity $\bar{\sigma}_{eff}$ is an invariant which is a function of the invariants J_2 and J_3 , where $J_3 = \frac{1}{3} \text{tr}(\boldsymbol{\tau}^{dev} \boldsymbol{\tau}^{dev} \boldsymbol{\tau}^{dev})$, and the invariant $\bar{\sigma}_{eff}$ is here chosen as

$$\bar{\sigma}_{eff} = \left(3J_2 + 3b \frac{J_3}{J_2^{3/2}} \right)^{1/2} \quad (42)$$

It should be noted that it is the parameter b that controls the influence of the J_3 invariant, i.e. the non-roundness of the transformation surface in the deviatoric plane, cf. Tomita and Iwamoto (2001) and Iwamoto and Tsuta (2002). If b is set to 0 the common effective stress according to von Mises is recovered. There are many different functions that yield surfaces which depend on J_3 . In the proposed model we have selected a function also used by Patoor *et al.* (1995). That developed by Krenk (1996) would have been another possibility.

Note finally that the evolution of \mathbf{l}^{tr} is obtained from (40) as

$$\text{sym}(\mathbf{l}^{tr}) = \dot{z} \frac{\partial h}{\partial \boldsymbol{\tau}} = K \left(\frac{3}{2} \frac{\partial \bar{\sigma}_{eff}}{\partial \boldsymbol{\tau}} + \frac{1}{3} \delta \mathbf{1} \right) \dot{z} \quad (43)$$

The proposed model has many similarities with the models developed by Fischer *et al.* (1997), Leblond *et al.* (1989) and Leblond (1989). The transformation condition, (36), which is based on thermodynamic forces bear a close resemblance to the one proposed by Fischer *et al.* (1997), the main difference lying in the form of evolution chosen for the transformation strain. Whereas Fischer *et al.* (1997) used an evolution found from a micromechanical viewpoint, the evolution in the present model is a pure continuum formulation. Although no specific form for F_{trans} is considered here, several different formulations exist, cf. Patoor *et al.* (1995) and Fischer *et al.* (1997, 1998). The approach taken here is to determine directly F_{trans} on the basis of experimental data. Obviously suitable properties need to be incorporated into F_{trans} in order for a realistic response to be obtained. This will be demonstrated in a later section.

5 Model calibration

The model presented involves several material parameters that need to be calibrated against results of experimental testing. The procedure employed is complicated due to the fact that a satisfactory model calibration has to rely on experimental data which contains both the evolution of the yield stress and the corresponding evolution of a martensitic phase at several different temperatures. Such comprehensive information regarding the development of a martensitic phase in austenitic steels is scarce in the existing literature. A stainless steel of grade AISI304, which is a Ni-Cr steel, will be used here as a prototype material and the experimental data provided by Onyuna (2003) will be considered.

The transformation surface, as already mentioned, is assumed to be dependent on the J_3 -invariant. The degree of deviation from a circular surface in the deviatoric plane is controlled by the parameter b in (42). A calibration of b to results from experimental tests would require multiaxial test data. Such data has unfortunately not been found in the literature on stainless steel. However, an approximate calibration of b can be performed in crystallographic terms. Fischer *et al.* (1997) and Huang (1999) describe transformation conditions that are similar to (15) and (16), the difference being in \mathbf{h} . In the present formulation, \mathbf{h} is based on a phenomenological evolution of the transformation strains. In Fischer *et al.* (1997) and in Huang (1999), \mathbf{h} is the additional strain that occurs in a micro-region due to the transformation of the microstructure from austenite into martensite.

To obtain the initial shape of the transformation surface, a situation in which no plastic stress has developed is considered. Moreover, consider first a single crystal in which an interface exists between the martensite and the austenite. During martensite growth this interface defines the front of the martensite phase. The deformation gradient related to this growth is given by

$$\mathbf{A} = \mathbf{1} + \epsilon \mathbf{n} \otimes \mathbf{p} \quad (44)$$

which can be determined on the basis of knowledge of the direction of the habit plane, \mathbf{p} , the direction of the deformation, \mathbf{n} , and the magnitude of the deformation, ϵ . The associated transformation strain is given by

$$\mathbf{E}^{tr} = \frac{1}{2} (\mathbf{A}^T \mathbf{A} - \mathbf{1}) \quad (45)$$

Note that the transformation condition for a crystal involves several planes due to lattice symmetry and is here, in line with Huang (1999), given as

$$h_I = \mathbf{S} : \mathbf{R}_I \mathbf{E}^{tr} \mathbf{R}_I^T - k \leq 0 \quad (46)$$

where k correspond to a transformation threshold value and \mathbf{S} is the second Piola-Kirchhoff stress tensor. The different symmetry variants of the martensite phase, described by the rotation tensor \mathbf{R}_I , are given by the cubic Laue group, cf. Hane and Shield (1998).

Since most materials consist of multiple grains and an isotropic model is desired, a polycrystalline transformation condition is more useful than a single crystal formulation, such as in (46). One of the easier ways of obtaining a polycrystalline transformation condition – a method adopted by e.g. Huang (1999) and Lexcellent and Blanc (2004) – is to assume that transformation takes place as soon as the transformation condition is fulfilled in one single grain, i.e.

$$h = \max_{\substack{I \in 1..24 \\ J \in 1..n}} \left(\mathbf{S} : \mathbf{R}_J^c \mathbf{R}_I \mathbf{E}^{tr} \mathbf{R}_I^T \mathbf{R}_J^{c,T} \right) - k \leq 0 \quad (47)$$

here it is assumed that the crystals exhibit certain orientations described by the rotation tensor \mathbf{R}_J^c , where the subscript J denotes a specific crystal. J takes on integer values from 1 to n , and n is the total number of crystals.

Obviously, taking advantage of the above formulation requires that the deformation tensor \mathbf{A} be established. Several experimental tests are available through which the habit plane normal and the magnitude and direction of the deformation can be identified. For example in Dunne and Wayman (1971) \mathbf{p} , \mathbf{n} and ϵ are determined experimentally for Fe-7.9Cr-1.1C, giving $\mathbf{p} = (0.363, 0.854, 0.373)$, $\mathbf{n} = (-0.195, 0.607, -0.771)$ and $\epsilon = 0.185$. This is not exactly the same steel as that considered here, but the habit plane is correct and both the resulting shear deformation and the volumetric change are in line with findings for Ni-Cr steels.

In Figure 1 the calibration of (41) to the transformation surface obtained by (47) is shown, it is being assumed that $\boldsymbol{\tau} \approx \mathbf{S}$ holds approximately as initial phase transformation is considered. The transformation surface is determined by use of 1000 randomly oriented grains. As Figure 1a shows, the calibration in the deviatoric plane of $b = 0.35$ in (42) is found to fit quite well. In Figure 1b the calibration of δ in the meridian plane with $\delta = 0.29$ is shown. Since it is only the shape of the transformation surface that determines b and δ the axes in both figures are normalized.

Having determined the shape of the transformation surface, it is possible to identify and calibrate $F_{trans}(z, \theta)$ and the stress/strain curves as well. Unfortunately these can not be decoupled. Both due to lack of data and since sufficient accuracy was obtained, as will be shown, it is assumed that $H_a = H_m$. From (26b) it is found that $Q = 0$. Returning to (41), it is possible to calibrate $F_{trans}(z, \theta)/K(\theta)$ against experimental data containing the relation between the phase fraction z and the stress $\boldsymbol{\tau}$ through

$$\frac{F_{trans}(z, \theta)}{K(\theta)} = \left(\bar{\sigma}_{eff} + \frac{1}{3} \delta I_1 \right) \quad (48)$$

For a given temperature θ , and for different values of the logarithmic strain ϵ_{true} , it is noted that both the stress σ_{true} and the corresponding volume fraction of martensite can be identified from experimental data, cf. Figure 3. Approximating the Kirchhoff stress

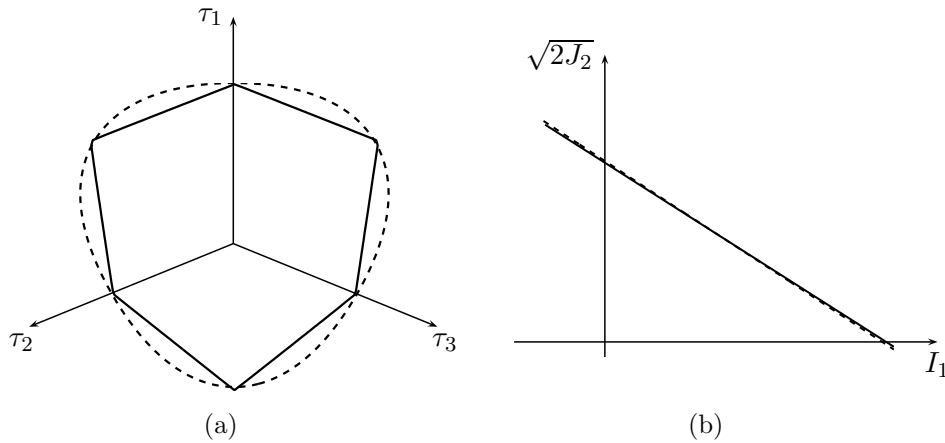


Figure 1: Determination of the transformation surface in the proposed model. The dashed lines represent the behavior of the proposed model. (a) Calibration of the b -parameter in the deviatoric plane. (b) Calibration of the δ -parameter in the meridian plane.

by σ_{true} in (48), F_{trans}/K can be estimated, and since z is known for this value of σ_{true} , a new graph of F_{trans}/K versus z can be obtained. The transformed data for different temperatures are shown in Figure 2. An advantage of a graph of this sort is that F_{trans}/K can be identified and calibrated. A suitable form of $F_{trans}(z, \theta)$ is found to be

$$\frac{F_{trans}(z, \theta)}{K(\theta)} = c_1(\theta) + c_2(\theta) [1 - \exp(-c_3 z)] [1 - c_4 \ln(1 - z)] \quad (49)$$

where c_1 , c_2 , c_3 and c_4 are parameters, a form for which rather close agreement between simulated and experimental results was obtained for the stainless steel that is considered. The combination of an exponential and a logarithmic function is chosen in order to obtain the required sigmoidal shape of the function $F_{trans}(z, \theta)$ where it is required that z asymptotically approach 1, cf. Figure 2. The exponential term will control the behavior at small values of z whereas the logarithmic term control the behavior as z approaches 1. The use of a logarithmic term can be found in e.g. Fischer *et al.* (1997) where it also satisfies the need of restricting z to the interval $0 \leq z \leq 1$. The parameters c_1 and c_2 in (49) are temperature-dependent. The values of these parameters, at different temperatures, are given in Table 1. It is also found that the parameters $c_3 = 25$ and $c_4 = 2$ may be kept constant, without any temperature dependence, which also applies to the constant $K = 0.185$.

It is also noted that if $\exp(-c_3 z) \approx 0$, i.e. for z close to 1, (49) can be rewritten. Based on (48) and (49), it then follows that

$$z = 1 - \exp \left[-\frac{1}{c_2 c_4} \left(\bar{\sigma}_{eff} + \frac{1}{3} \delta I_1 + c_1 - c_2 \right) \right] \quad (50)$$

and a generalized form of the renowned Koistinen and Marburger (1959) relation is obtained.

Table 1: Temperature dependence of the parameters contained in the transformation criteria.

Temperature	213 K	233 K	293 K	313 K
$c_1(\theta)$	290.0	330.0	610.0	680.0
$c_2(\theta)$	255.0	270.0	350.0	390.0

Since metallic materials are being considered here, the bulk and shear moduli are taken as $K_{bulk} = 167$ GPa and $G_{shear} = 77$ GPa, respectively. The initial yield stress of $\sigma_{y0}^a(\theta)$ for the austenite phase is calibrated as $\sigma_{y0}^a(213) = 310$ MPa, $\sigma_{y0}^a(233) = 300$ MPa, $\sigma_{y0}^a(293) = 230$ MPa and $\sigma_{y0}^a(313) = 200$ MPa for the temperatures considered. The hardening of the material is described by the parameters $R_\infty = 1200$ MPa and $H_a = H_m = 2500$ MPa, which are adjusted to fit the experimental data in question. The homogenization of the yield stress is achieved on the basis of a non-linear mixing relation according to (29), rewritten as

$$\sigma_{y0} = \overline{m}(z)\sigma_{y0}^a \quad \text{where} \quad \overline{m}(z) = 1 + m(z) \left(\frac{\sigma_{y0}^m}{\sigma_{y0}^a} - 1 \right) \quad (51)$$

where the form

$$\overline{m}(z) = 1 + [\exp(f_1 z) - 1] f_2 \quad (52)$$

is adopted. The factors f_1 and f_2 are material parameters to which values are given by calibrating the model against experimental data. For stainless steel $f_1 = 1.65$ and $f_2 = 0.79$ are found to yield a reasonable material behavior as the austenite progressively transforms into martensite. Figure 3 shows the response of the calibrated model as compared with the experimental results. The response of the model, as shown in Figure 3, is calculated using the numerical implementation discussed in Appendices A and B. The proposed model is clearly able to capture the features exhibited by the experimental data.

As indicated above, the present model obviously involve some material parameters controlling the behavior of the model. For convenience, the full set of parameters are summarized in Table 2. Their individual values are stated above when describing the calibration of the model at different temperatures.

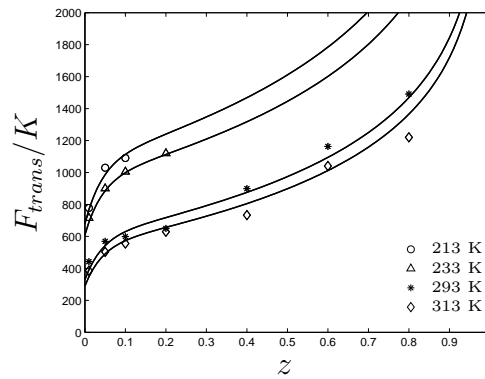


Figure 2: The function $F_{trans}(z, \theta)/K(\theta)$ and its temperature-dependence.

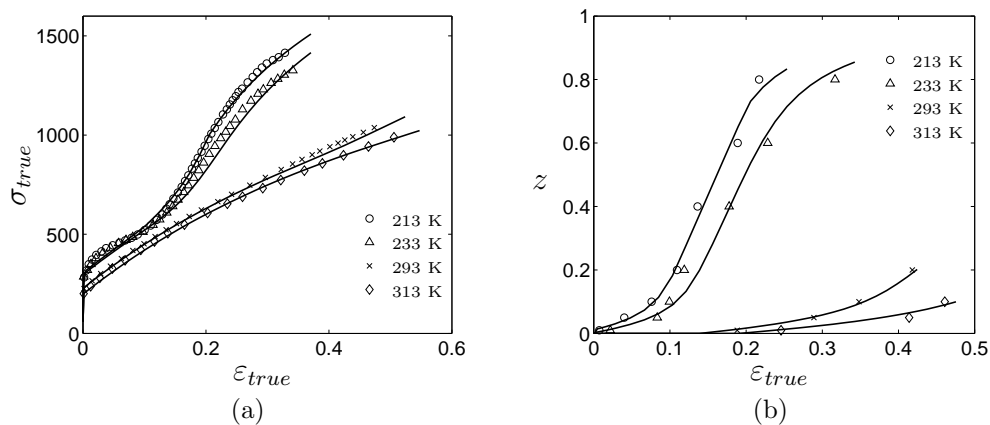


Figure 3: (a) The simulated stress-strain response (true stress in MPa). Results of the numerical simulations (solid lines) as compared with the experimental results (symbols). Results of uniaxial tension tests of AISI304 steel at different temperatures were taken from Onyuna (2003). (b) The volume fraction of martensite as a function of the true strain, corresponding to the graphs in (a).

Table 2: Summary of the material parameters that are used in the model.

K_{bulk}	Bulk modulus
G_{shear}	Shear modulus
H_a, H_m	Hardening moduli of the austenite and martensite phases, respectively
R_∞	Saturation hardening
$\sigma_{y0}^a(\theta), \sigma_{y0}^m(\theta)$	Initial yield stresses of the austenite and martensite phases, respectively
b	Parameter controlling the shape of the transformation surface
δ	Parameter controlling the volumetric phase transformation
$c_1(\theta), c_2(\theta)$	Parameters used to control the temperature dependence of the transformation criteria
c_3	Parameter used to control the behavior of the transformation criteria at small values of z
c_4	Parameter used to control the behavior of the transformation criteria at large values of z
K	Parameter in the transformation potential similar to the ‘‘Greenwood-Johnson’’-constant used by Berveiller and Fischer (1997)
f_1, f_2	Parameters in the homogenization of the initial yield stresses

6 Numerical examples

Two simulation examples are presented in this section to illustrate the usefulness of the proposed constitutive model. The numerical handling of the model, i.e. the integration of the constitutive relations and the formulation of an algorithmic tangent stiffness, is presented in Appendices A and B. The model is applied as a user-defined subroutine in the commercial finite element code Abaqus Standard.

6.1 Necking of a bar

In the first example, a cylindrical rod is exposed to tensile loading, cf. Figure 4. This simulation model is used to illustrate the influence of the phase transformation on the response of the material. A cylindrical rod with an aspect ratio of $l_0/r_0 = 3$ is modeled, where $2l_0$ is the initial length and r_0 the initial radius of the rod. A total of 3750 axisymmetric elements of the type CAX4 are used in the model. Taking advantage of the axisymmetry and in-plane symmetry that are present, only one fourth of the bar is analyzed. The tensile load is applied by controlling the displacement of one end of the specimen and to be able to observe localization phenomena, necking is triggered by introducing a small imperfection in the geometry. This is achieved through the radius being described as $r = r(\xi)$, where ξ is the axial position in the rod, such that

$$r(\xi) = r_0 \left[1 - \alpha \cos \left(\frac{\pi \xi}{2l_0} \right) \right] \quad (53)$$

Choosing $\alpha = 3 \times 10^{-4}$, the “waist” of the rod is reduced by 0.03 %. Additionally, the dimensions $l_0 = 9$ mm and $r_0 = 3$ mm are chosen. Figures 5 and 6 show the load-displacement curves with and without phase transformation.

Figures 5 and 6 show quite clearly the strong influence of the martensite phase on the response of the material. As indicated by theory and also by the experimental data shown in Figure 3, the effects of phase transformation become more pronounced as the temperature decreases. At the two lower temperatures – 213 K and 233 K – the martensite phase evolves rapidly as shown in Figure 3b. This is also evident in Figures 5 and 6. The localization of plastic deformation occurs almost at the same state of deformation, both with and without phase transformation since most of the martensite formation already has taken place. At the two higher temperatures – 293 K and 313 K – the behavior is somewhat different. The growth of a martensitic phase there is much slower and the ultimate martensite content is lower for the same displacement. The plastic localization at these temperatures is markedly delayed due to the formation of martensite. When localization is initiated in the plastically deformed material, further austenite is transformed into martensite and rapidly stabilizes the region of localization through increased hardening.

Figures 7 and 8, finally, show the evolution of the martensite phase in the tensile specimen at $\theta = 213$ K and $\theta = 293$ K. One can clearly see that during necking, the martensite distribution is more homogeneous at the lower of the two temperatures. This is due to almost all the austenite having been transformed into martensite at this stage, whereas at higher temperatures additional transformation is possible to a greater extent.

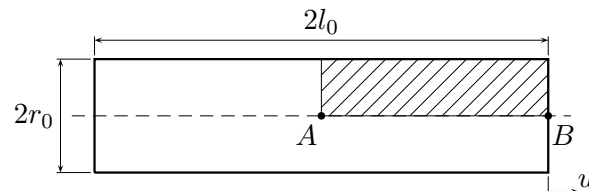


Figure 4: Geometry of the simulation model representing a cylindrical rod exposed to tensile loading. Taking advantage of the symmetry, only one fourth of the rod is actually analyzed (the hashed region). Points A and B are used for reference. The tensile load is applied by enforcing a displacement u of one end of the bar.

6.2 Deep-drawing of a cup

The second example concerns a deep-drawing process similar to the one presented in Takuda *et al.* (2003). As can be seen in Figure 9, the diameter and the profile radius of the punch are $d_1 = 60$ mm and $r_1 = 6$ mm and those of the die $d_2 = 65$ mm and $r_2 = 6$ mm, respectively. The initial blank thickness is chosen as $t = 1$ mm and the initial

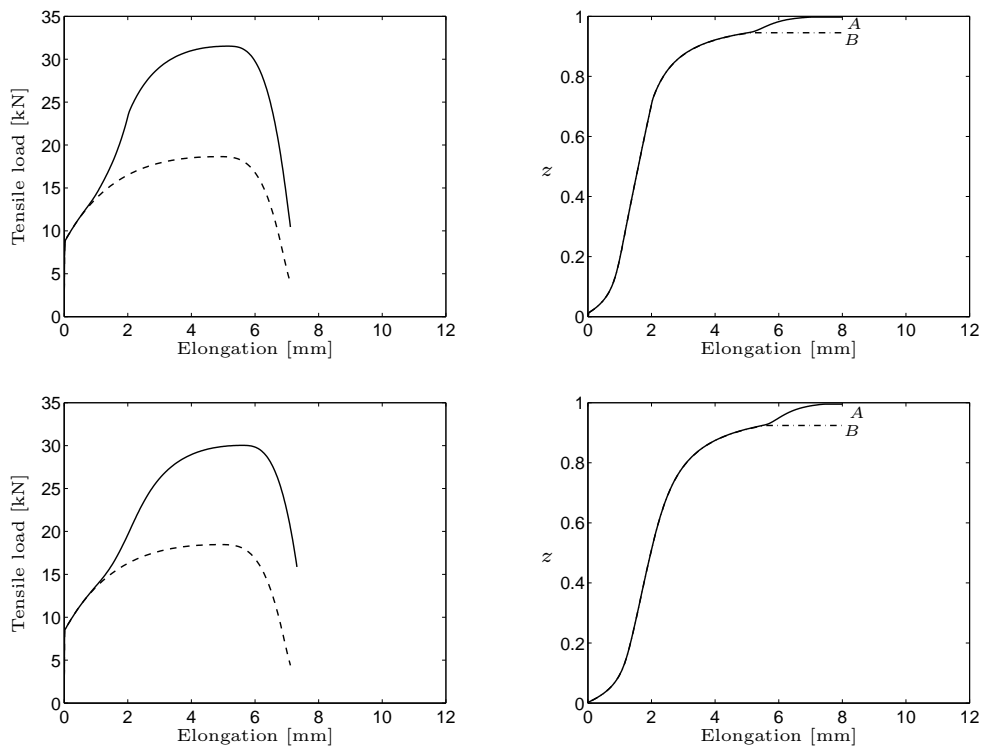


Figure 5: Simulated response of an axisymmetric bar exposed to tensile loading. The two graphs at the left show the response both with phase transformation (solid lines) and without (dashed lines). The two graphs at the right show the corresponding evolution of martensite at the center end points of the simulated geometry, cf. Figure 4. The dash-dotted lines are related to the end point B of the rod and the solid lines are related to the center point A of the rod. The two rows of graphs are taken at the temperatures (taken from the top row and down) $\theta = 213$ K and $\theta = 233$ K. Figure 6 shows the corresponding information for the temperatures $\theta = 293$ K and $\theta = 313$ K, respectively.

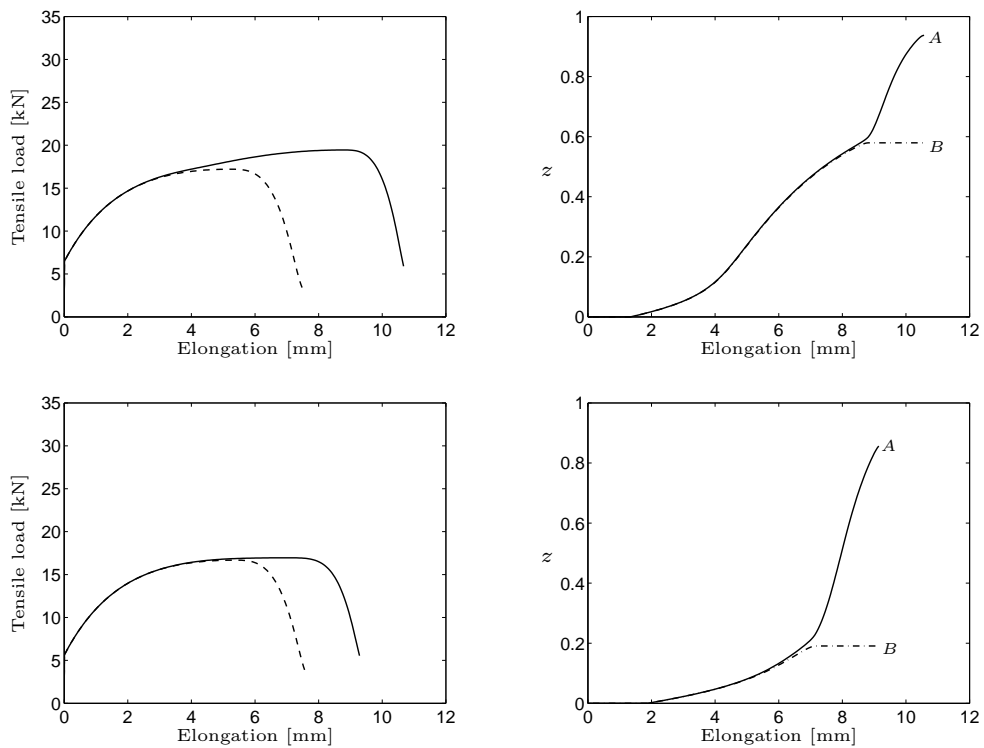


Figure 6: Figure 5 continued, here for the temperatures $\theta = 293$ K (top) and $\theta = 313$ K (bottom).

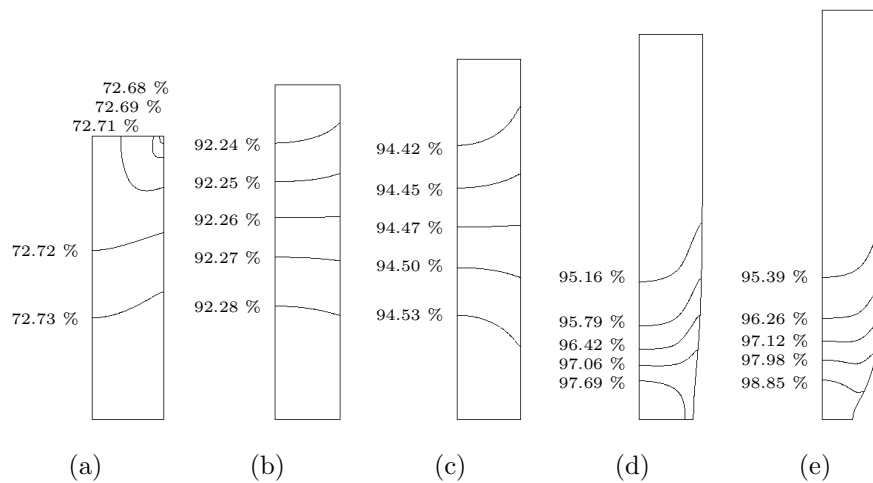


Figure 7: Evolution of the martensite phase in an axially loaded circular bar at $\theta = 213$ K for differing states of elongation: (a) 2 mm, (b) 4 mm, (c) 5 mm, (d) 6 mm and (e) 7 mm.

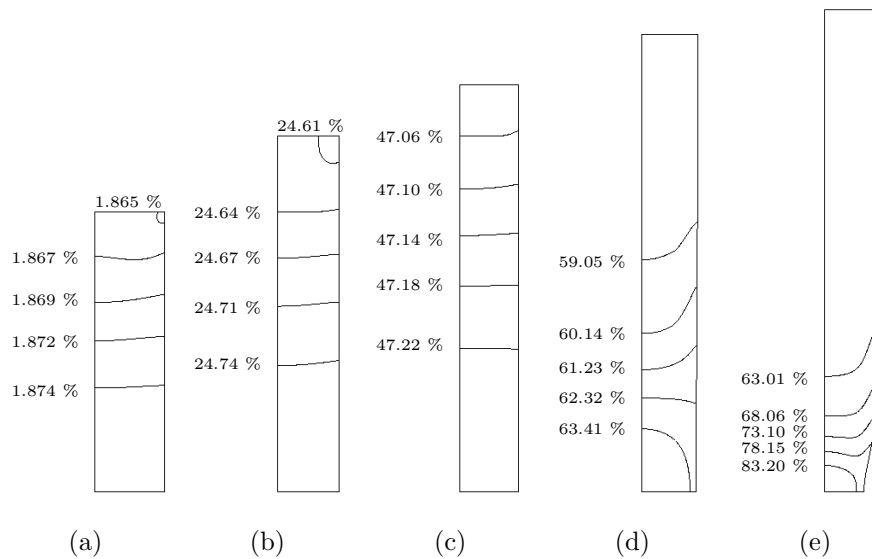


Figure 8: Evolution of the martensite phase in an axially loaded circular bar at $\theta = 293$ K for differing states of elongation: (a) 2 mm, (b) 5 mm, (c) 7 mm, (d) 9 mm and (e) 10 mm.

blank diameter is taken as $d_3 = 152$ mm, giving a deep-drawing ratio of $d_3/d_1 \approx 2.53$. These dimensions correspond to those used in Takuda *et al.* (2003) and according to this model setup, a blank holder is also modeled onto which a force of 4 kN is applied. The coefficient of friction is chosen as 0.15 between the blank and the punch and 0.1 at all other contacting surfaces. This is in line with what is used by Serri *et al.* (2005). To reduce the computational effort, an axisymmetric analysis is performed. A total of 3200 elements of the type CAX4 is used to represent the metal plate and the thickness of the plate is resolved by eight layers of elements.

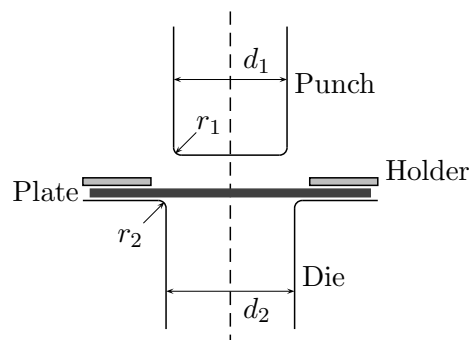


Figure 9: The simulated deep-drawing setup.

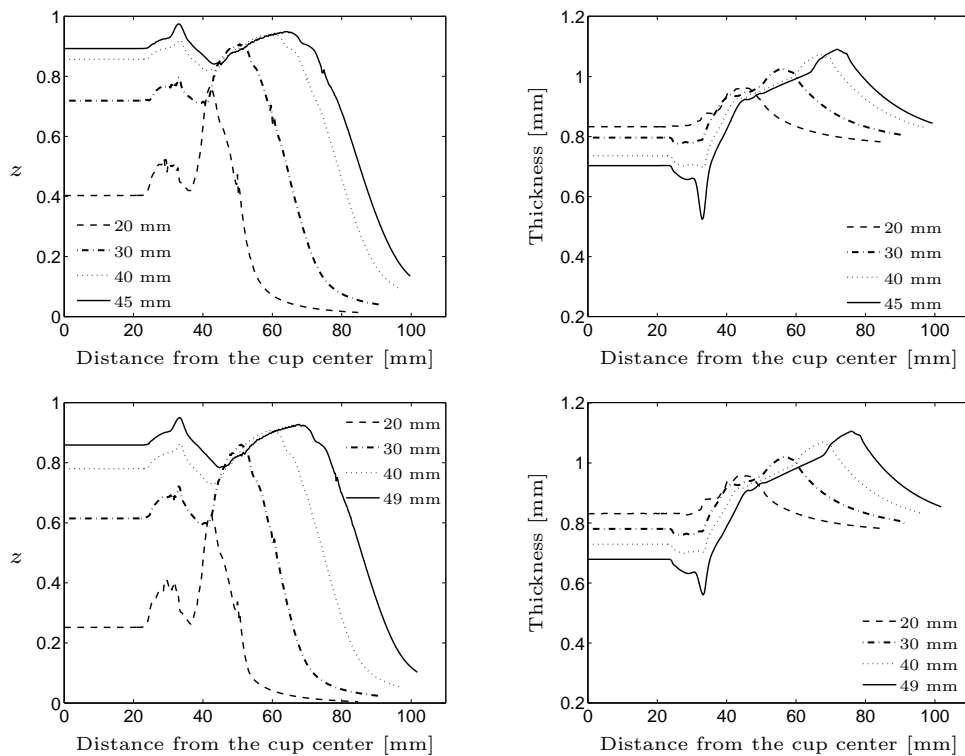


Figure 10: The left graphs to the left show the martensite distribution in the cup at various stages of deformation, whereas the graphs to the right illustrate the variation in thickness of the plate at the corresponding states of deformation. The upper two figures show a cup drawn at $\theta = 213$ K and the bottom two figures a cup drawn at $\theta = 233$ K. Note that in both figures the horizontal axes show the distance along the deformed plate.

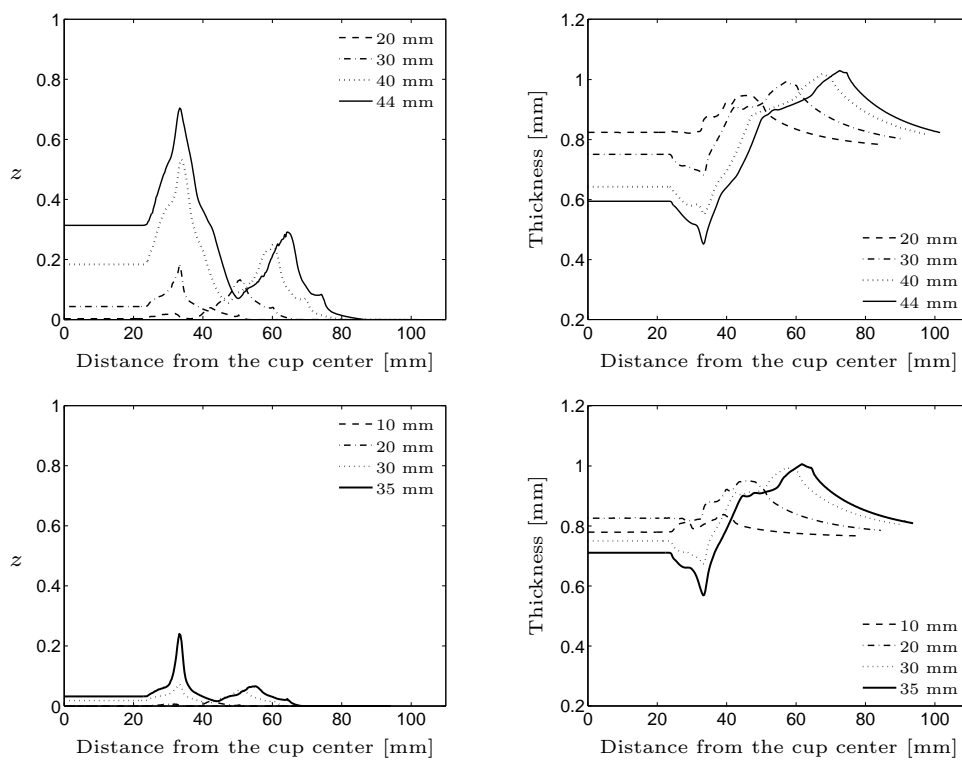


Figure 11: Figure 10 continued, here for the temperatures $\theta = 293$ K (top) and $\theta = 313$ K (bottom).

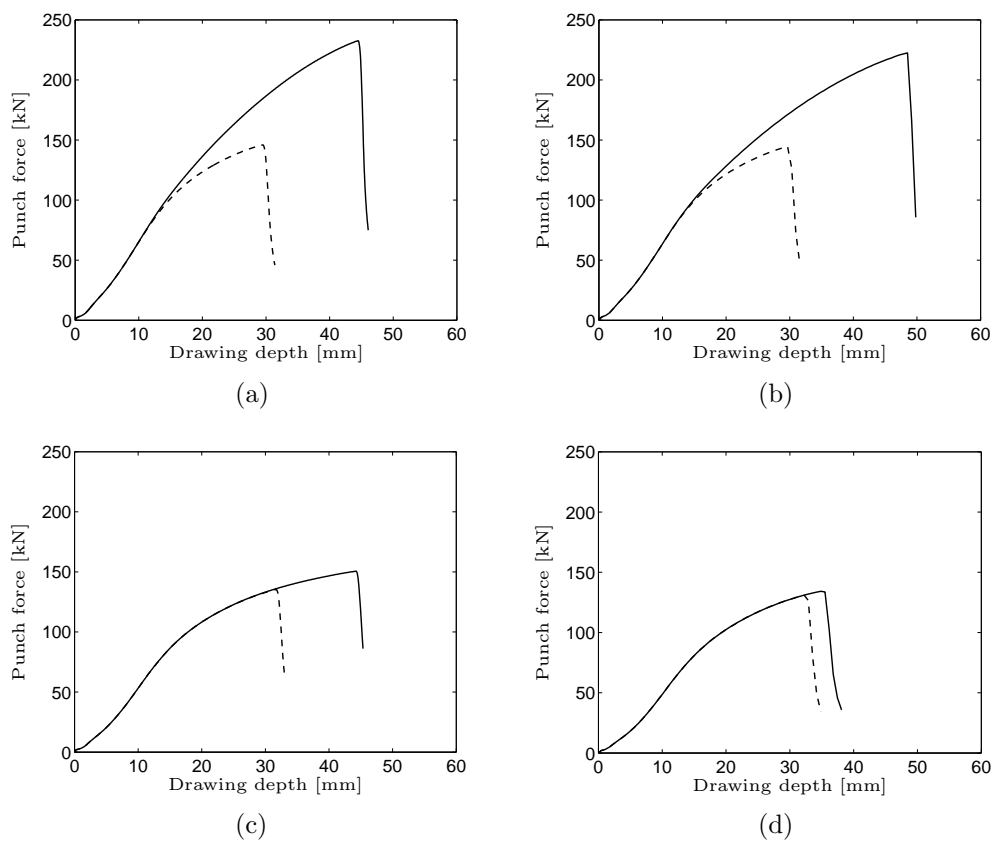


Figure 12: Force-displacement curves for the deep-drawing process both with phase transformation (solid lines) and without (dashed lines) at the four temperatures considered: (a) $\theta = 213$ K, (b) $\theta = 233$ K, (c) $\theta = 293$ K and (d) $\theta = 313$ K.

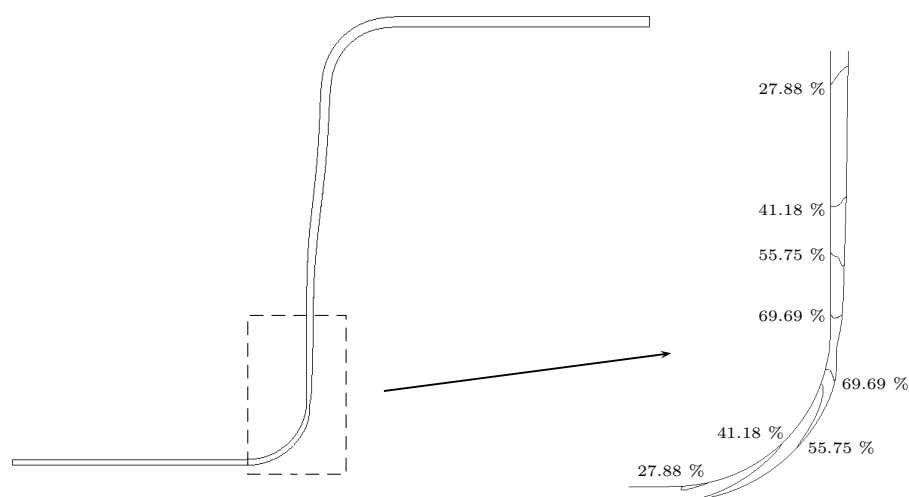


Figure 13: Global shape of the deep-drawn cup at deformation localization and a close-up on the corresponding martensite distribution in the region of localization. The deformation shown is that obtained at temperature $\theta = 293$ K and drawing-depth 45.4 mm.

The simulated martensite distribution in the drawn cup is shown in Figures 10 and 11 at each of the four considered temperatures for different drawing depths. The tendency for there to be two peaks in the martensite distribution is similar to what is found in Takuda *et al.* (2003) and in Serri *et al.* (2005). Note that the horizontal axes in these figures show the distance in the deformed plate, this explaining the horizontal shift of the curves in each graph. Figures 10 and 11 also show the variation in thickness of the cup wall at the same drawing depths. For each temperature, the largest drawing depth shown corresponds to the deformation state at evident localization. These localization points are also clearly visible in Figure 12, where force-displacement curves are shown for the four temperatures considered. The material response, both in the presence (solid lines) and the absence (dashed lines) of martensite, can be seen. Note that the localization occurs close to the bottom profile radius of the cup. This region exhibits severe material thinning and often displays subsequent fracture, characteristic of deep-drawing processes of the sort studied here, cf. Takuda *et al.* (2003) and Serri *et al.* (2005). A more detailed presentation of this localization is shown in Figure 13 at $\theta = 293$ K. In Figures 10 and 11 a slight increase in sheet thickness is evident where the metal is still caught between the die and the plate holder.

Comparing the results of the simulation of the cup drawing with the previous results for the necking of a cylindrical bar reveals certain differences. At $\theta = 233$ K, necking occur more or less at the same elongation, regardless of whether a martensitic phase is present or not. The same behavior is also observed for $\theta = 213$ K. In contrast, in the cup-drawing example, the localization is delayed markedly due to the influence of the martensitic phase.

This can be interpreted in the way that during cup drawing a stress state exists that allows martensite to form and to stabilize the region of localization. This results in an increase in the formability of the sheet metal somewhere in the temperature interval of 233 K to 293 K.

7 Concluding remarks

Increasing attention is being directed at austenitic steels undergoing martensitic transformation. This is due in no small part to the fact that use of shape-memory alloys and so-called TRIP steels are becoming increasingly common. The transformation from austenite to martensite has appealing traits, such as the high rate at which the transformation occurs and the possibility to obtain a material with inhomogeneous ductility, making these steels interesting in practical applications. The martensite phase has a yield stress that surpass that of the austenite phase by several orders of magnitude. This makes it possible to influence the localization of plastic deformation for example in forming operations, e.g. by controlling the temperature of the tooling.

The present paper proposes a constitutive model for austenitic steels that progressively transform into martensite. The model is set within a thermodynamically consistent finite plasticity framework. It is shown through calibration against several isothermal experiments that the influence of temperature on the transformation is satisfactorily captured. The proposed model renders a robust simulation tool, suitable for large-scale simulations of diffusionless phase transformation in austenitic steel. The implementation of the model is convenient since it is found that only two additional equations are needed as compared to standard J_2 -plasticity models with isotropic hardening. The qualities of the proposed model are demonstrated in two numerical examples, the necking of a bar and a cup deep-drawing process. Comparisons are made with experimental results found in the literature with satisfactory agreement being obtained.

The model is described in some detail, together with an outline of procedures for integrating the constitutive relations and calculating the algorithmic stiffness tensor. Procedures for calibrating the model against experimental data are also described.

8 Acknowledgments

Håkan Hallberg gratefully acknowledges the funding provided by the ProViking program Simu-Net-Shape under grant SFF V03.22.

A Integration of the constitutive model

The integration of the constitutive equations is performed by use of a Euler backward scheme. For achieving this, it was found to be advantageous to first derive the evolution

of the left Cauchy-Green tensor \mathbf{b}^e . Recall the expressions (3) and (4) which permit the formulation

$$\dot{\mathbf{F}}^{ir} = \mathbf{F}^{e-1} \mathbf{l}^{ir} \mathbf{F}^e \mathbf{F}^{ir} \tag{54}$$

Separating this relation into an isochoric – i.e. volume-preserving – and a volumetric part, results in

$$\begin{aligned} \dot{\mathbf{F}}_i^{ir} &= \mathbf{F}_i^{e-1} \mathbf{l}^{ir,dev} \mathbf{F}_i^e \mathbf{F}_i^{ir} \\ \frac{d}{dt} [\ln (J^{ir})] &= \text{tr} (\mathbf{l}^{ir}) \end{aligned} \tag{55}$$

where the notation $(\cdot)_i$ was introduced to denote isochoric quantities, e.g. $\mathbf{F}_i^e = J^{-\frac{1}{3}} \mathbf{F}^e$.

Having retrieved the above quantities, one can then calculate the Lie derivative of the isochoric tensor \mathbf{b}_i^e according to

$$\begin{aligned} \mathcal{L}\mathbf{b}_i^e &= \mathbf{F}_i \frac{\partial}{\partial t} (\mathbf{F}_i^{-1} \mathbf{b}_i^e \mathbf{F}_i^{-T}) \mathbf{F}_i^T = \\ &= \mathbf{F}_i \frac{\partial}{\partial t} (\mathbf{F}_i^{ir-1} \mathbf{F}_i^{ir-T}) \mathbf{F}_i^T = -2\text{sym} (\mathbf{l}^{ir,dev} \mathbf{b}_i^e) \end{aligned} \tag{56}$$

use being made of

$$\mathbf{l}^{ir} \mathbf{b}^e = -\mathbf{F} \frac{\partial}{\partial t} (\mathbf{F}^{ir-1}) \mathbf{F}^{ir-T} \mathbf{F}^T \tag{57}$$

Following Simo and Hughes (2000), the integration of the constitutive relations is performed by applying a Euler backward scheme to \mathbf{C}_i^{ir-1} , where $\mathbf{C}_i^{ir} = (\mathbf{F}_i^{ir})^T \mathbf{F}_i^{ir}$. This allows (56) to be rewritten as

$$\dot{\mathbf{C}}_i^{ir-1} = -2\mathbf{F}_i^{-1} \text{sym} (\mathbf{l}^{ir,dev} \mathbf{b}_i^e) \mathbf{F}_i^{-T} \tag{58}$$

The integration is performed by use of the following expression, which relates the step n and the subsequent step $n + 1$ that between them span the interval Δt

$$\mathbf{C}_i^{ir-1} - (\mathbf{C}_i^{ir-1})_n = -2\mathbf{F}_i^{-1} \text{sym} (\mathbf{l}^{ir,dev} \mathbf{b}_i^e) \mathbf{F}_i^{-T} \Delta t \tag{59}$$

where all quantities not indicated are calculated at the state $n + 1$. A reformulation is then made in terms of \mathbf{b}_i^e according to

$$\mathbf{b}_i^e = \mathbf{b}_i^{e,trial} - 2\text{sym} (\mathbf{l}^{ir,dev} \mathbf{b}_i^e) \Delta t \tag{60}$$

where the trial quantity $\mathbf{b}_i^{e,trial} = \mathbf{F}_i (\mathbf{C}_i^{ir-1}) \mathbf{F}_i^T$ is identified. Taking advantage of the isochoric relative deformation gradient \mathbf{f}_i the following relations are obtained

$$\mathbf{b}_i^{e,trial} = \mathbf{f}_i (\mathbf{b}_i^e)_n \mathbf{f}_i^T, \quad \mathbf{f}_i = \mathbf{F}_i (\mathbf{F}_i^{-1})_n \tag{61}$$

Assuming that $(\mathbf{b}_i^e)_n$ is isochoric, it follows that $\mathbf{b}_i^{e,trial}$ is also isochoric. Since \mathbf{l}^{tr} and \mathbf{b}_i^e commute, (60) can be reformulated as

$$\mathbf{b}_i^{e,trial} = (\mathbf{1} + 2\mathbf{l}^{ir,dev} \Delta t) \mathbf{b}_i^e \tag{62}$$

Careful investigation reveals, however, that the volume-preserving property of \mathbf{b}_i^e is biased by the Euler backward scheme, requiring that one ensure that the volume preserving property of the update operator $(\mathbf{1} + 2\mathbf{l}^{ir,dev} \Delta t)$ is enforced – i.e. $\det(\mathbf{b}_i^e) = 1$ is required to hold. Introducing a simple scaling allows the following expression to be obtained

$$\frac{\mathbf{1} + 2\mathbf{l}^{ir,dev} \Delta t}{\det(\mathbf{1} + 2\mathbf{l}^{ir,dev} \Delta t)} \mathbf{b}_i^e = \mathbf{b}_i^{e,trial} \tag{63}$$

in which it is recognized that \mathbf{b}_i^e is an isochoric quantity. The volumetric term $\frac{d}{dt} [\ln(J^{ir})] = \text{tr}(\mathbf{l}^{ir})$ is integrated through

$$\ln(J^{ir}) - \ln(J^{ir})_n = \text{tr}(\mathbf{l}^{ir}) \Delta t \tag{64}$$

Equations (64) and (63) now fully define the evolution of \mathbf{F}^{ir} . It should be recalled in passing that \mathbf{l}^{ir} consists of both a plastic component and a component related to the phase transformation. Explicitly, this means that

$$\mathbf{l}^{ir} = \mathbf{l}^p + \mathbf{l}^{tr} = \mathbf{l}^{p,dev} + \mathbf{l}^{tr,dev} + \frac{1}{3} \text{tr}(\mathbf{l}^{tr}) \mathbf{1} \tag{65}$$

Use of (63) together with the previously derived evolution laws shown in (13) and (17) allows a residual function $\mathcal{R}_{\mathbf{b}^e}$ to be defined. Similarly a residual function \mathcal{R}_{J^p} can be determined from (64). On basis of the yield function f and a Euler backward integration of both (13b) and the transformation potential h , additional residual functions can be found that complete the following system of equations

$$\begin{aligned} \mathcal{R}_{\mathbf{b}^e} &= \mathbf{b}_i^{e,trial} - \frac{\mathbf{1} + 2\mathbf{l}^{p,tr} \Delta t + 2\mathbf{l}^{tr,dev} \Delta t}{\det(\mathbf{1} + 2\mathbf{l}^{p,tr} \Delta t + 2\mathbf{l}^{tr,dev} \Delta t)} \mathbf{b}_i^e = \mathbf{0} \\ \mathcal{R}_{J^{ir}} &= -\ln(J^{ir}) + \ln(J_n^{ir}) + \text{tr}(\mathbf{l}^{tr}) \Delta t = 0 \\ \mathcal{R}_f &= \sigma_{eff} - \sigma_{y0} - R = 0 \\ \mathcal{R}_g &= \Delta\kappa - \Delta\lambda \left(1 - \frac{R}{R_\infty}\right) = 0 \\ \mathcal{R}_h &= \left(\bar{\sigma}_{eff} + \frac{1}{3}\delta I_1\right) - \{c_1(\theta) + c_2(\theta) [1 - \exp(-c_3z)] [1 - c_4 \ln(1 - z)]\} = 0 \end{aligned} \tag{66}$$

where the subscripts n and $n+1$ were dropped for sake of clarity and where $\Delta\kappa = \kappa_{n+1} - \kappa_n$. It should be emphasized that in adopting the system shown in (66) only two scalar equations

enter due to phase transformation, in addition, the system conserves the property $\det(\mathbf{b}_i^e) = 1$. For convenience the total residual and the iterative quantities are collected in \mathcal{R} and $\mathbf{Y} = [\mathbf{b}_i^e \quad J^e \quad \Delta\lambda \quad \kappa \quad z]$, respectively. The system of equations is then solved using the Newton-Raphson scheme, for which the updating procedure is given schematically by

$$\mathbf{Y} := \mathbf{Y} + \Delta\mathbf{Y} \quad \text{where} \quad \Delta\mathbf{Y} = - \left(\frac{\partial \mathcal{R}}{\partial \mathbf{Y}} \right)^{-1} \mathcal{R} \quad (67)$$

This approach to integration of the constitutive relations is discussed e.g. by Håkansson *et al.* (2005). In order to increase the efficiency of the solution scheme, the number of equations in (66) can be reduced by taking into account the coaxiality between \mathbf{b}^e , \mathbf{l}^{tr} and $\boldsymbol{\tau}$, cf. Håkansson *et al.* (2006).

B Consistent tangent modulus

If the algorithmic tangent stiffness tensor \mathbf{D}^{ATS} is calculated in the material configuration and is then pushed forward to the spatial configuration, the resulting expression assumes the form

$$\mathbf{D}^{ATS} = 2(\mathbf{F} \overline{\otimes} \mathbf{F}) : \frac{\partial \mathbf{S}}{\partial \mathbf{C}} : (\mathbf{F}^T \overline{\otimes} \mathbf{F}^T) \quad (68)$$

where $\mathbf{S} = \mathbf{F}^{-1} \boldsymbol{\tau} \mathbf{F}^{-T}$ is the second Piola-Kirchhoff stress tensor and where, for arbitrary second-order tensors \mathbf{A} and \mathbf{B} , the operation $(\mathbf{A} \overline{\otimes} \mathbf{B})_{ijkl} = A_{ik} B_{jl}$ is defined. The minor symmetry of \mathbf{D}^{ATS} is used in the calculations, but is not written explicitly. In terms of this definition of \mathbf{D}^{ATS} , the tangential stiffness tensor can be expressed as

$$\mathbf{D}^{ATS} = -\mathbf{1} \overline{\otimes} \boldsymbol{\tau} - \mathbf{1} \underline{\otimes} \boldsymbol{\tau} + \frac{\partial \boldsymbol{\tau}}{\partial \mathbf{F}} \mathbf{F}^T \quad (69)$$

where the notation $(\mathbf{A} \underline{\otimes} \mathbf{B})_{ijkl} = A_{il} B_{jk}$ was introduced, again for the arbitrary second-order tensors \mathbf{A} and \mathbf{B} . Since the Kirchhoff stress tensor is assumed to depend on the Jacobian J^e of the elastic deformation gradient and the isochoric part \mathbf{b}_i^e of the left Cauchy-Green tensor – i.e. $\boldsymbol{\tau} = \boldsymbol{\tau}(J^e, \mathbf{b}_i^e)$ – the last term in (69) can be expressed as

$$\begin{aligned} \frac{\partial \boldsymbol{\tau}}{\partial \mathbf{F}} \mathbf{F}^T &= \frac{\partial \boldsymbol{\tau}}{\partial J^e} \left(\frac{\partial J^e}{\partial J^{e,trial}} \frac{\partial J^{e,trial}}{\partial \mathbf{F}} + \frac{\partial J^e}{\partial \mathbf{b}_i^{e,trial}} \frac{\partial \mathbf{b}_i^{e,trial}}{\partial \mathbf{F}} \right) \mathbf{F}^T + \\ &\frac{\partial \boldsymbol{\tau}}{\partial \mathbf{b}_i^e} : \left(\frac{\partial \mathbf{b}_i^e}{\partial \mathbf{b}_i^{e,trial}} \frac{\partial \mathbf{b}_i^{e,trial}}{\partial \mathbf{F}} + \frac{\partial \mathbf{b}_i^e}{\partial J^{e,trial}} \frac{\partial J^{e,trial}}{\partial \mathbf{F}} \right) \mathbf{F}^T \end{aligned} \quad (70)$$

It is important to note that only spatial quantities such as \mathbf{b}_i^e and $\mathbf{b}_i^{e,trial}$ are obtained via the post-multiplication of \mathbf{F}^T . From (70) it can be recognized that the differentiations

$\frac{\partial b_i^e}{\partial \mathbf{X}}$ and $\frac{\partial J^e}{\partial \mathbf{X}}$, where $\mathbf{X} = [b_i^{e,trial} \quad J^{e,trial}]$, need to be obtained. This can be achieved by recalling that \mathbf{X} drives the system defined by (66), i.e. that

$$\mathcal{R} = \mathcal{R}(\mathbf{Y}(\mathbf{X}), \mathbf{X}) = \mathbf{0} \quad \forall \mathbf{X} \quad (71)$$

This makes it possible to perform the operation

$$\frac{\partial \mathbf{Y}}{\partial \mathbf{X}} = - \left(\frac{\partial \mathcal{R}}{\partial \mathbf{Y}} \right)^{-1} : \frac{\partial \mathcal{R}}{\partial \mathbf{X}} \quad (72)$$

in which the only non-zero terms are $\frac{\partial \mathcal{R}_{b^e}}{\partial b_i^{e,trial}}$ and $\frac{\partial \mathcal{R}_{J^e}}{\partial J^{e,trial}}$. Note that there is no need to evaluate the Jacobian $\frac{\partial \mathcal{R}}{\partial \mathbf{Y}}$ again since it was already used to solve (66). These results make all components of the algorithmic tangent stiffness tensor \mathbf{D}^{ATS} available.

References

- Berveiller, M. and Fischer, F. D., editors (1997). *Mechanics of Solids with Phase Changes*. Number 368 in CISM Courses and Lectures. Springer Wien New York.
- Cherkaoui, M., Berveiller, M., and Lemoine, X. (2000). Coupling between plasticity and martensitic phase transformation: overall behavior of polycrystalline trip steels. *International Journal of Plasticity*, **16**, 1215–1241.
- Dunne, D. P. and Wayman, C. M. (1971). The crystallography of ferrous materials. *Metallurgical Transactions*, **2**, 2327–2341.
- Fischer, F. D., Oberaigner, E. R., and Tanaka, K. (1997). A micromechanical approach to constitutive equations for phase changing materials. *Computational Materials Science*, **9**, 56–63.
- Fischer, F. D., Oberaigner, E. R., Tanaka, K., and Nishimura, F. (1998). Transformation induced plasticity, revised and updated formulation. *International Journal of Solids and Structures*, **35**, 2209–2227.
- Fischer, F. D., Reisner, G., Werner, E., Tanaka, K., Cailletaud, G., and Antretter, T. (2000). A new view on transformation induced plasticity (TRIP). *International Journal of Plasticity*, **16**, 723–748.
- Ganghoffer, J. F., Denis, S., Gautier, E., Simon, A., Simonsson, K., and Sjöström, S. (1991a). Mechanical and thermodynamical study of a macroscopically coherent phase transition. Case of the martensitic transformation. *Journal de Physique IV*, **1**, 89–94.

- Ganghoffer, J. F., Denis, S., Gautier, E., Simon, A., Simonsson, K., and Sjöström, S. (1991b). Micromechanical simulation of a martensitic transformation by finite elements. *Journal de Physique IV*, **1**, 77–82.
- Garion, C., Skoczen, B., and Sgobba, S. (2006). Constitutive modelling and identification of parameters of the plastic strain-induced martensitic transformation in 316L stainless steel at cryogenic temperatures. *International Journal of Plasticity*, **22**, 1234–1264.
- Giusti, J. (1981). *Contraintes et Déformations Résiduelles d'Origine Thermique; Application au Soudage et à la Trempe des Aciers*. Ph.D. thesis, Université Paris VI.
- Greenwood, G. W. and Johnson, R. H. (1965). The deformation of metals under small stresses during phase transformations. *Proceedings of the Royal Society*, **283 A**, 403–422.
- Håkansson, P., Wallin, M., and Ristinmaa, M. (2005). Comparison of isotropic hardening and kinematic hardening in thermoplasticity. *International Journal of Plasticity*, **7**, 1435–1460.
- Håkansson, P., Wallin, M., and M.Ristinmaa (2006). Thermomechanical response of non-local porous material. *International Journal of Plasticity*, **22**(11), 2066–2090.
- Hane, K. F. and Shield, T. W. (1998). Symmetry and microstructure in martensites. *Philosophical Magazine A*, **78**(6), 1215–1252.
- Harrysson, M. and Ristinmaa, M. (2006). Description of evolving anisotropy at large strains. *Mechanics of Materials*, *in press*.
- Huang, W. (1999). “Yield” surfaces of shape memory alloys and their application. *Acta Materialia*, **47**(9), 2769–2776.
- Idesman, A. V., Levitas, V. I., Preston, D. L., and Cho, J.-Y. (2005). Finite element simulations of martensitic phase transitions and microstructures based on a strain softening model. *Journal of the Mechanics and Physics of Solids*, **53**, 495–523.
- Iwamoto, T. and Tsuta, T. (2002). Computational simulation on deformation behavior of CT specimens of TRIP steel under mode I loading for evaluation of fracture toughness. *International Journal of Plasticity*, **18**(11), 1583–1606.
- Koistinen, D. P. and Marburger, R. E. (1959). A general equation prescribing the extent of the austenite-martensite transformation in pure iron-carbon alloys and plain carbon steels. *Acta Metallurgica*, **7**, 59–60.

- Krenk, S. (1996). Family of invariant stress surfaces. *Journal of Engineering Mechanics*, **122**(3), 201–208.
- Kröner, E. (1960). Allgemeine kontinuumstheorie der versetzungen. *Arch. Rational Mech. Anal.*, pages 273–334.
- Leblond, J. B. (1980). Simulation Numérique du Soudage – Modélisation Mathématique des Transformations Métallurgiques – Etat d’Avancement des Travaux. Technical Report TM/C DC/80.066, Framatome.
- Leblond, J. B. (1989). Mathematical modelling of transformation plasticity in steels II: Coupling with strain hardening phenomena. *International Journal of Plasticity*, **5**, 573–591.
- Leblond, J. B., Mottet, G., and Devaux, J. C. (1986a). A theoretical and numerical approach to the plastic behaviour of steels during phase transformations - i. derivation of general relations. *Journal of the Mechanics and Physics of Solids*, **34**(4), 395–409.
- Leblond, J. B., Mottet, G., and Devaux, J. C. (1986b). A theoretical and numerical approach to the plastic behaviour of steels during phase transformations - ii. study of classical plasticity for ideal-plastic phases. *Journal of the Mechanics and Physics of Solids*, **34**(4), 411–432.
- Leblond, J. B., Devaux, J., and Devaux, J. C. (1989). Mathematical modelling of transformation plasticity in steels I: Case of ideal-plastic phases. *International Journal of Plasticity*, **5**, 551–572.
- Lee, E. H. and Liu, D. T. (1967). Finite strain plasticity particularly for plane waves. *Journal of Applied Physics*, **38**, 19–27.
- Levitas, V. (1997). Thermomechanical theory of martensitic phase transformation in inelastic materials. *International Journal of Solids and Structures*, **35**, 889–940.
- Levitas, V., Idesman, A. V., Olson, G. B., and Stein, E. (2002). Numerical modelling of martensitic growth in a elastoplastic material. *Philosophical Magazine A*, **82**(3), 429–462.
- Levitas, V. I., Idesman, A. V., and Olson, G. B. (1998). Continuum modeling of strain-induced martensitic transformation at shear-band intersections. *Acta Materialia*, **47**(1), 219–233.
- Lexcellent, C. and Blanc, P. (2004). Phase transformation yield surface determination for some shape memory alloys. *Acta Materialia*, **52**, 2317–2324.

- Magee, C. L. (1969). The nucleation of martensite. *ASM International, Materials Park*, pages 115–155.
- Müller, C. and Bruhns, O. T. (2006). A thermodynamic finite-strain model for pseudoelastic shape memory alloys. *International Journal of Plasticity*, **22**, 1658–1682.
- Olson, G. B. and Cohen, M. (1975). Kinetics of strain-induced martensitic nucleation. *Metallurgical Transactions*, **6A**, 791–795.
- Onyuna, M. O. (2003). *Deformation behaviour and martensitic transformations in metastable austenitic steels and low alloyed multiphase steels*. Ph.D. thesis, Department of Materials Science and Technology, Freiberg University of Mining and Technology.
- Patoor, E., Amrani, M. E., Eberhardt, A., and Berveiller, M. (1995). Determination of the origin for the dissymmetry observed between tensile and compressive tests on shape memory alloys. *Journal de Physique IV*, **5**, 495–500.
- Petit-Grostabussiat, S., Taleb, L., and Jullien, J.-F. (2004). Experimental results on classical plasticity of steels subjected to structural transformations. *International Journal of Plasticity*, **20**(8-9), 1371–1386.
- Serri, J., Martiny, M., and Ferron, G. (2005). Finite element analysis of the effects of martensitic phase transformation in trip steel sheet forming. *International Journal of Mechanical Sciences*, **47**, 884–901.
- Simo, J. C. and Hughes, T. J. R. (2000). *Computational Inelasticity*. Springer-Verlag, second edition.
- Simonsson, K. (1994). *Micro-mechanical FE-simulations of the plastic behaviour of steels undergoing martensitic transformation*. Ph.D. thesis, Linköping.
- Sjöström, S. (1982). *The calculation of quench stresses in steel*. Ph.D. thesis, Linköping.
- Sjöström, S. (1985). *Numerical Methods in Thermal Problems*, pages 1189–1202. Pineridge Press.
- Stringfellow, R. G., Parks, D. M., and Olson, G. B. (1992). A constitutive model for transformation plasticity accompanying strain-induced martensitic transformation in metastable austenitic steels. *Acta Metallurgica et Materialia*, **40**(7), 1703–1716.
- Takuda, H., Mori, K., Masachika, T., Yamazaki, E., and Watanabe, Y. (2003). Finite element analysis of the formability of an austenitic stainless steel sheet in warm deep drawing. *Journal of Materials Processing Technology*, **143-144**, 242–248.

- Taleb, L. and Sidoroff, F. (2003). A micromechanical modeling of the Greenwood-Johnson mechanism in transformation induced plasticity. *International Journal of Plasticity*, **19**(10), 1821–1842.
- Tanaka, K., Oberaigner, E. R., and Fischer, F. D. (1994). A unified theory on thermo-mechanical mesoscopic behaviour of alloy materials in the process of martensitic transformation. *Mechanics of Phase Transformations and Shape Memory Alloys (ASME)*, **AMD 189/PVP 292**, 151–157.
- Tanaka, K., Oberaigner, E. R., and Fischer, F. D. (1996). Kinetics on the micro- and macro-levels in polycrystalline alloy materials during martensitic transformation. *Acta Mechanica*, **116**, 171–186.
- Tomita, Y. and Iwamoto, T. (1995). Constitutive modeling of trip steel and its application to the improvement of mechanical properties. *International Journal of Mechanical Sciences*, **37**, 1295–1305.
- Tomita, Y. and Iwamoto, T. (2001). Computational prediction of deformation behavior of trip steels under cyclic loading. *International Journal of Mechanical Sciences*, **43**, 2017–2034.
- Turteltaub, S. and Suiker, A. S. J. (2005). A multiscale thermomechanical model for cubic to tetragonal martensitic phase transformations. *International Journal of Solids and Structures*, **43**, 4509–4545.
- Wolff, M., Böhm, M., and Schmidt, A. (2006). Modelling of steel phenomena and their interactions – an internal variable approach. *Materialwissenschaft und Werkstofftechnik*, **37**(1), 147–151.